STRUCTURAL DESIGN AND EXPERIMENTAL ANALYSIS OF A NEW LOCAL CUTTING AND GRINDING DEVICE

Yong CHEN[1,2,*], Wenxin PU[1], Zhen ZHANG[3], Ping XIONG[1], Zhaoran ZHANG[1]

To address the current challenges of tedious operations, low efficiency, and poor quality in cutting and grinding pipes, this paper presents the structural design of a local cutting and grinding device for DN500 pipes. This device can simultaneously cut pipes and groove grinding with a diameter of 406-508 mm and wall thickness under 25 mm. After optimizing the lifting mechanism, the maximum deformation was reduced to 0.144 mm and the maximum stress to 128.66 MPa, which is only 54.6% of the pre-optimization value, achieving a safety factor of 2.76. Modal analysis confirmed structural stability, and kinematic simulation verified operational requirements. Experimental results show a 40% reduction in operation time compared to manual methods, demonstrating the device's precise positioning and high work efficiency.

Keywords: Cutting and grinding; Structural design; Structural optimization; Modal analysis; Kinematic simulation

1. Introduction

With the rapid development of large-diameter, high-grade steel oil and gas pipes in various countries [1], numerous aging and failure issues have also become increasingly prominent [2], leading to a rise in the frequency of safety incidents [3]. In addition to planned maintenance and renovations, oil and gas pipes must also conduct emergency repair operations in response to unforeseen accidents during media transportation [4]. Pipe maintenance ensures safe operations and merits further exploration [5].

Due to restrictions on on-site construction, including obstructed views, operational inconveniences, and safety risks [6], ensuring welding quality becomes challenging. Various degrees of circumferential weld defects persist, such as dents and scratches [7-8]. Additionally, the locations of these welding defects must be cut and ground to create a weld groove for re-welding [9]. The quality of the pipe welding is a critical factor influencing the overall quality of the project [10-11].

* Corresponding author
[1] School of Mechatronic Engineering, Southwest Petroleum University, Chengdu 610500, Sichuan, China, e-mail address: swpucy1412@163.com.
[2] Oil and Gas Equipment Technology Sharing and Service Platform of Sichuan Province.
[3] Gas Transmission Management Department of PetroChina Southwest Oil and Gasfield Company, Chengdu, China, e-mail address: 2374516945@qq.com.

The grooving machine and pipe end grooving lathe produced by Gubbiotti are designed for small to medium-sized pipes [12]. Baihuamei proposed using an electric variable frequency grooving machine with a gas-cutting torch [13]. Additionally, A. G. Demeissie developed a spiral welded pipe grinding machine capable of simultaneously grinding the pipe's inner and outer surfaces [14]. However, these processing methods are limited cum, cumbersome to operate, and lack efficiency. Currently, most of the equipment used on construction sites is designed and manufactured based on a fixed pipe type [15], which can lead to positioning errors. Therefore, it is essential to conduct an integrated design of a local cutting and grinding device and accurately locate the defect position of the pipe before operation [16-17].

Given the challenges associated with tedious operations, restricted working space, and poor grinding quality, this paper presents a new integrated local cutting and grinding device for steel pipes to meet welding standards.

2. Structural design and operating principle

The local cutting and grinding device consists of a circumferential motion mechanism, an axial motion mechanism, a lifting motion mechanism, and a deflection motion mechanism. The detailed structural composition is shown in Figure 1. The cutter is a crucial component of the cutting and grinding process. Given the advantages of V-groove processing, which is convenient and conducive to welding, this paper selects a 60° V-shaped alloy cutter with 10 teeth, capable of grinding high-grade steel. The frame is primarily based on the existing external matching device structure, enhanced with the addition of a movable disc, gears, a screw, and other components.

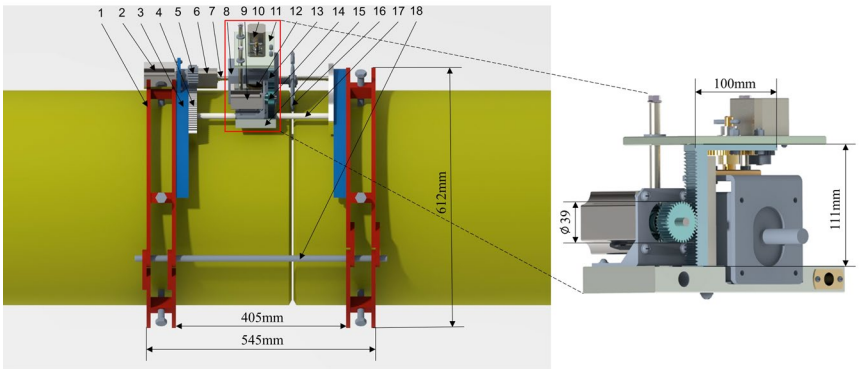

1—Pipe clamp; 2—Circumferential drive motor; 3—Stationary disc; 4—Movable disc; 5—Driving gear; 6—Axial drive motor; 7—Screw; 8—Grinding motor; 9—Lifting drive motor; 10—Deflection drive motor; 11—Lifting plate; 12—Deflecting spindle; 13—Lifting rack; 14—Lifting gear; 15—Moving plate; 16—Cutting and grinding tool; 17—Support rod; 18—Centering rod

Fig. 1. Diagram of each movement structure

The screw is made of 304 stainless steel. The support rod, gear, and centering rod are made of 42CrMo, while the remaining components are made of 45 steel. The material properties are shown in Table 1.

Table 1

Material properties

Materials	Density (g/cm^3)	Young's Modulus (GPa)	Poisson's Ratio	Yield Strength (MPa)
304 stainless steel	7.93	190	0.3	205
42CrMo	7.75	210	0.3	950
45 steel	7.85	207	0.3	355

The master controller and driver are EmbedFire's STM32F407 and EBF-MSD4805, respectively. The circumferential and lifting motors are 57HS22, paired with the corresponding reducers, PLF60J-L1-7 and PLF60J-L1-4, with rated torques of 15.4 N·m and 8.8 N·m, respectively. The axial and deflection motors are of type 42HS08, with a rated torque of 0.72 N·m. The grinding motor is DZM-53/00-SCF32, with a 4.77 N·m rated torque.

The circumferential movement is driven by a motor-operated pinion gear that meshes with the movable disc, enabling the movable disc to traverse along the circumferential groove of the stationary disc. The axial movement is facilitated by a motor-driven screw, with the support rod connected to the axially moving plate to maintain stability. The lifting movement is powered by a motor-driven lifting gear, which drives the rack vertically, causing the grinding motor to ascend and descend. The motor driving the deflection spindle through two gears achieves deflection within a specified angle. The control process is as follows: the master controller transmits pulse signals to the driver, delivering current to each stepper motor and ensuring smooth cutting and grinding processes, as shown in Figure 2.

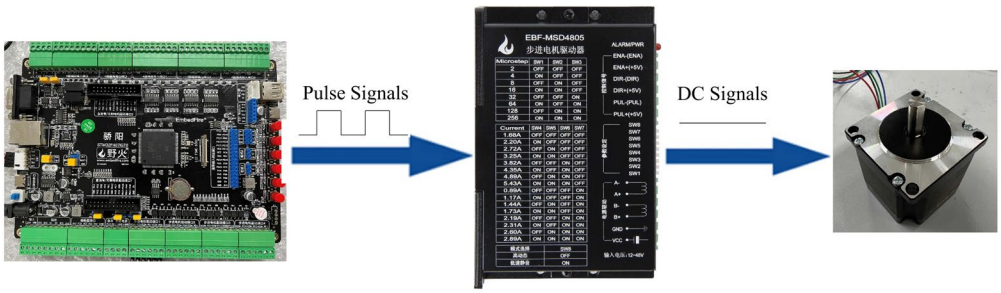

Fig. 2. Control principle when the device is in operation

Table 2 presents the dimensional gauge data of the device using an X80 pipe with a diameter of 508 mm and a wall thickness of 14 mm, along with a cutter with a diameter of 150 mm.

Table 2

Dimensional gauges of the device

Parameters	Data
inner diameter of the frame (mm)	532
overall device weight (kg)	62
circumferential sliding distance (mm)	210
axial sliding distance (mm)	102
lifting height (mm)	34
maximum feed (mm)	25
maximum deflection angle (°)	±6.18

3. Kinematic and dynamic analysis

3.1 Strength check of key components

The lifting movement is accomplished by meshing the gear with the rack. The primary loads include the force exerted by the grinding motor, the weight of the lifting device, and the reaction force, all concentrated at the gear and rack meshing point. It is essential to conduct strength assessments on its key components.

The gear has 24 teeth with a tooth width of 25 mm. The width of the rack is 22 mm. Both components have a module of 1.5 mm, a pressure angle of 20°, and an accuracy level of 7. The material properties of the gear and rack are shown in Table 1. The total number of meshes is 373,935, and it has been verified that the mesh independence falls within a reasonable range, and the mesh quality is rated at 0.83. It has been densified at the tooth contact positions. The finite element pre-processing setup involves defining the gear-rack contact interface with no-separation contact, while the gear shaft is constrained as a fixed support. For the groove contact surface, displacement constraints are applied: the Z-axis (tangential direction) is free, whereas the X-axis (axial direction) and Y-axis (radial direction) are fixed at zero.

The mass analysis results in Creo simulations indicate that the total mass of the components in the lifting mechanism is approximately 14 kg. The radial reaction force is estimated at around 200 N, while the tangential reaction force is approximately 50 N. The reaction force exerted by the tool is concentrated at the contact point between the tool and the pipe; therefore, it should be modeled as a remote force load in ANSYS simulations to represent the actual working conditions more accurately.

When the machine head is positioned at the top of the frame, the rotation of the grinding tool generates a reaction force that acts radially, accompanied by a tangential component. The deformation and stress distribution maps are shown in Figure 3-a and 3-b. When the machine head is situated at the side of the frame, the gravitational force on the lifting mechanism aligns in the same or opposite direction as the tangential component of the reaction force during grinding, while the radial

reaction force is directed outward from the pipe. The deformation and stress distribution diagrams are presented in Figure 3-c and 3-d. When the machine head is located at the bottom of the frame, the radial component of the gravitational force acting on the lifting mechanism is equivalent to the radial component of the reaction force during grinding, while the tangential component of the reaction force continues to act in the tangential direction. The deformation and stress distribution diagrams are depicted in Figure 3-e and 3-f.

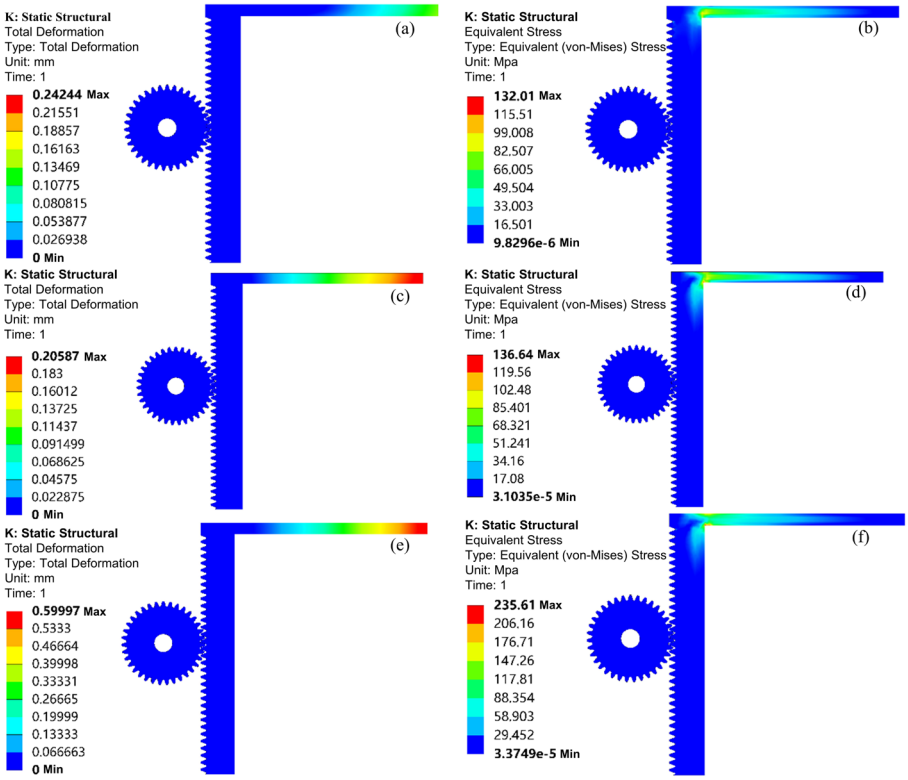

Fig. 3. Deformation and stress maps of the machine head at the top, side, and bottom of the frame, respectively

It can be observed from Figure 3 that when the machine head is positioned at the bottom of the frame, both deformation and stress reach their maximum levels. The maximum deformation recorded is about 0.6 mm, while stress is concentrated at the bottom edge of the rack corner, with a peak stress of approximately 235.61 MPa. This value is below the yield strength of 355 MPa. However, given that the corner is a welded joint, there is a potential risk of strength failure under actual working conditions. Additionally, as the upper top plate experiences deformation under pressure, 30° inclined ribs with a thickness of 3 mm have been added to the front and rear sides of the lower edge of the upper top plate. The structural integrity has been verified based on actual working conditions, as shown in Figure 4.

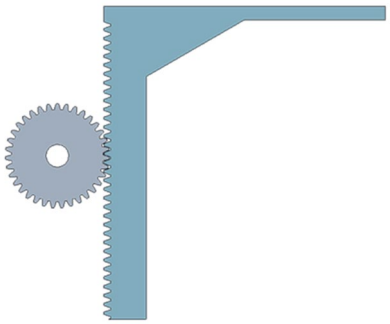

Fig. 4. Optimized structural model

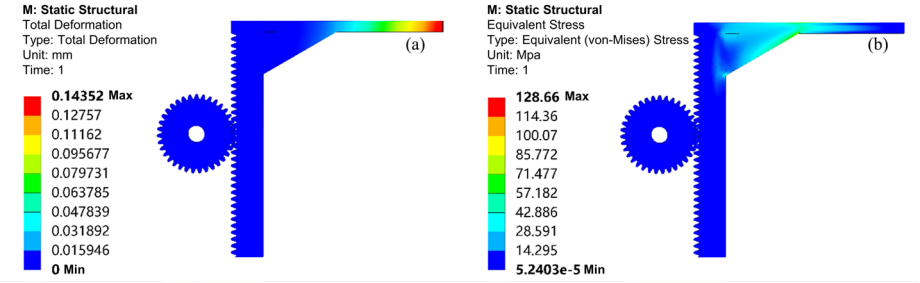

Fig. 5. Deformation and stress maps after optimization

After optimization, the maximum deformation has been reduced to approximately 0.144 mm, while the maximum stress is concentrated at the junction between the stiffener and the upper plate of the rack, measuring around 128.66 MPa, as shown in Figure 5. This value represents only 54.6% of the stress before optimization, resulting in a safety factor of 2.76.

3.2 Modal analysis of frame

The frame supports the weight of the grinding device during the cutting and grinding process. However, vibrations during work can lead to resonance and even collapse of the grinding device system. The frame is secured with 12 bolts, necessitating a modal analysis to ensure that its natural frequency range does not overlap with the motor's input frequency.

The motor that significantly impacts the frame is primarily the grinding motor, which operates at a speed of 3000 r/min. The exciting frequency of the motor on the frame at this speed is as follows:

$$f = \frac{un}{60i} \tag{1}$$

Take i = 1 and calculate it according to Equation (1). The frequencies are 50 Hz, 100 Hz, 150 Hz, 200 Hz, 250 Hz, and 300 Hz, listed in order.

Prior to modal analysis, the frame structure was systematically simplified, excluding bolts and some transmission components. The frame's component-specific material properties are shown in Table 1. The total number of meshes is

1,665,738, and it has been verified that the mesh independence falls within a reasonable range. The mesh quality is rated at 0.83. During the pre-processing stage in ANSYS simulations, the frame and twelve bolt surfaces at both ends of the frame are designated as fixed supports.

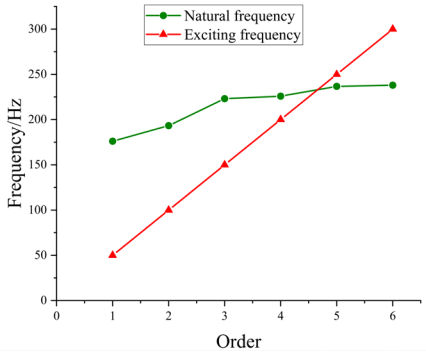

Fig. 6. A comparison of the natural frequency of the frame with the excitation frequency

As shown in Figure 6, the excitation frequency correlates with the natural frequency, suggesting that the frame may experience resonance, which could impact its regular operation. Consequently, optimizing the structure of specific frame components is essential to ensure their stability.

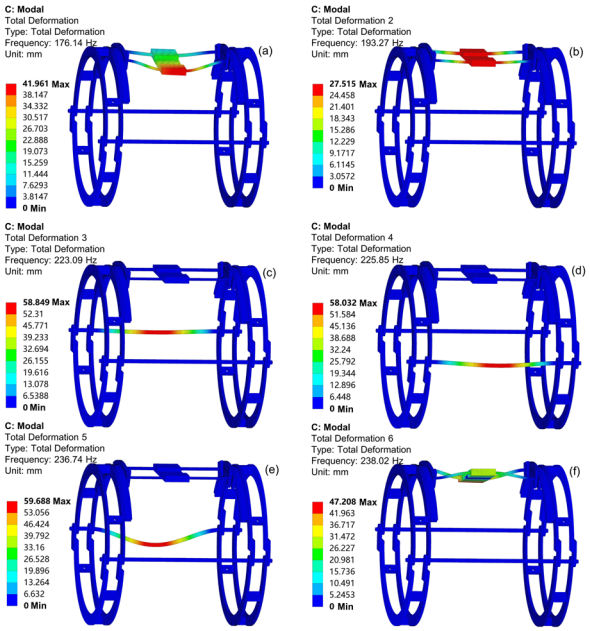

Fig. 7. The frequency response of the frame, where panels (a) through (f) correspond to the first through sixth orders, respectively

Figure 7 shows that the bending of the screw and support rod along the z-axis primarily characterizes the first and second-mode shapes. In contrast, the third

and fourth mode shapes are defined by bending the rear and front centering rods along the y-axis, respectively. The fifth mode shape is characterized by the bending of the rear centering rod along the z-axis, while the sixth mode shape again features the bending of the screw and support rod along the z-axis. The deformation is concentrated in these four components.

To mitigate resonance frequencies and enhance the stability of the frame, the lengths of the four members were reduced by 68 mm. The adjusted lengths are as follows: 600 mm for the centering rod, 350 mm for the screw (including the length of the motor body), and 350 mm for the support rod. The diameter was increased to 12 mm, and the corresponding aperture of the axial movement plate, through which the support rod passes, was also enlarged to 12 mm.

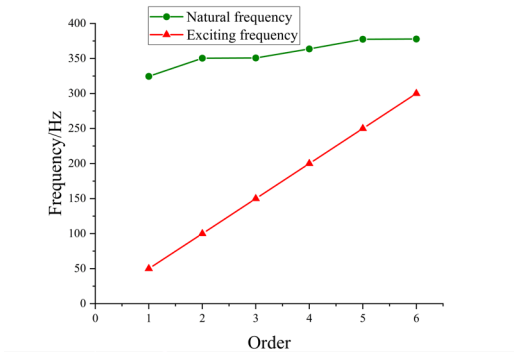

Fig. 8. Frequency comparison after optimization

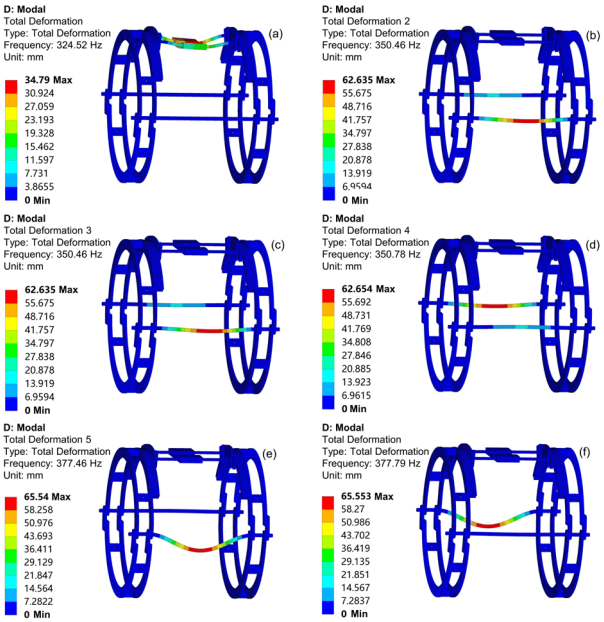

Fig. 9. The frequency mode shapes of the optimized frame for each order, where (a)–(f) correspond to the first through sixth orders, respectively

The simulation results in Figures 8 and 9 demonstrate that the optimized structure exhibits no resonance behavior, satisfying the stability requirements.

3.3 Verification of torque and force

When the machine head is located at the top of the frame, the movable disc will be subjected to the head's self-weight and the radial and tangential reaction forces caused by the tool's rotation. Based on the assembly's mass analysis in Creo simulations, the effective load is 30 kg (G=294 N), with a radial reaction force of about 200 N and a tangential reaction force of about 50 N.

During the simulation analysis in Adams, the grinding motor remains stationary. A radial reaction force of F1 = 200 N and a tangential reaction force of F2 = 50 N are applied at the point of contact between the tool and the pipe. Since circumferential motion is simulated through restraint and no coupling pair is introduced, the resistance to circumferential motion cannot be directly simulated. The inner radius of the frame is 266 mm, with a friction coefficient of 0.12. Using the formula $T = \mu \cdot N \cdot r$, the resulting resistance torque is calculated to be about 9.38 N·m. Consequently, a resistance torque ranging from 8 N·m to 10 N·m is applied to the circumferential motion motor to account for the effects of the machine head's weight and frictional resistance.

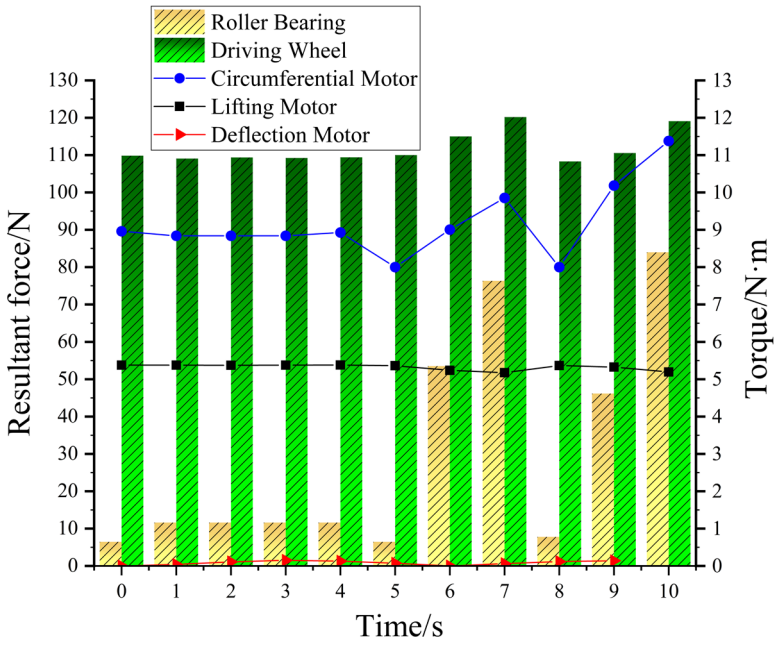

Fig. 10. Torque and stress diagram with the head at the top

As shown in Figure 10, The maximum torque of the circumferential and lifting motors is 11.38 N·m and 5.38 N·m, respectively. Additionally, the maximum torque that the deflection motor must overcome to remain stationary is about 0.15

N·m, less than the rated torque of each drive motor. The maximum radial force acting on the roller bearing during circumferential movement is approximately 84 N, and the maximum force exerted on the driving wheel during lifting movement is about 120.5 N. These forces are below the theoretical limits of 106.4 N and 133.6 N, respectively.

When the head is positioned at the side of the frame, the applied force and torque situations are identical to those when the head is located at the top of the rack.

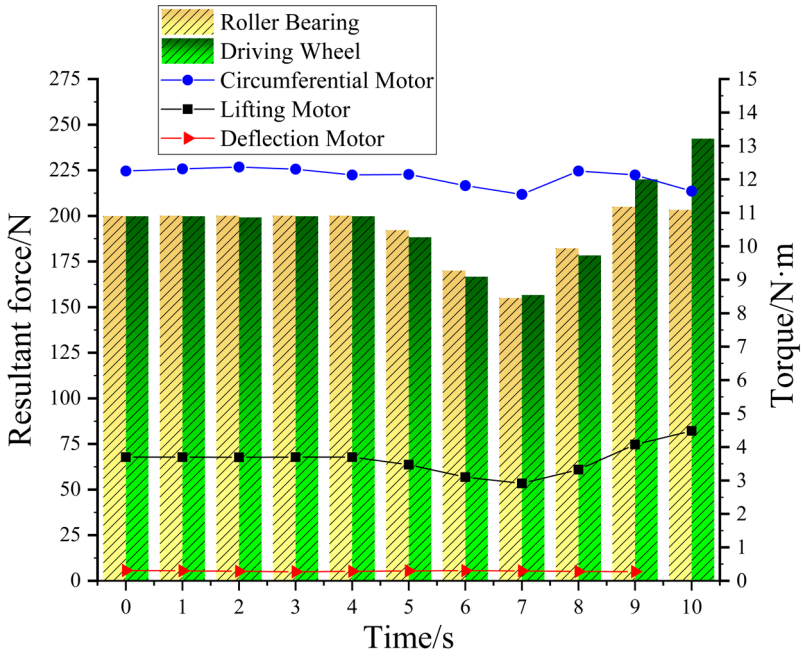

Fig. 11. Torque and stress diagram with the head at the side

As shown in Figure 11, the maximum torque of the circumferential and lifting motors is 12.38 N·m and 4.48 N·m, respectively. Additionally, the maximum torque that the deflection motor must overcome to remain stationary is about 0.306 N·m, less than the rated torque of each drive motor. The maximum radial force acting on the roller bearing during circumferential movement is approximately 205 N, and the maximum force exerted on the driving wheel during lifting movement is around 237 N. Both forces are below the theoretical limits of 264.6 N and 242.3 N, respectively.

When the head is positioned at the bottom of the frame, the applied force and torque situations are identical to those when the head is located at the top of the rack.

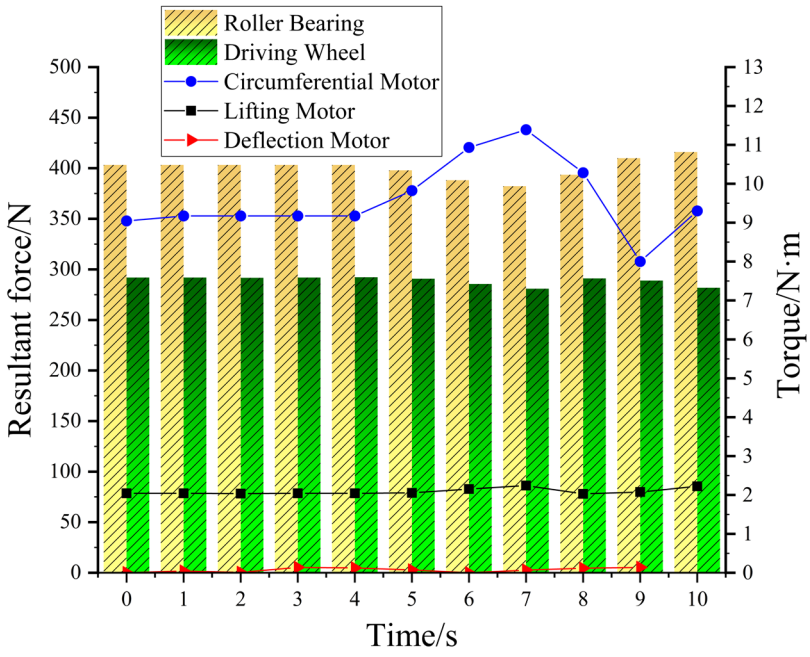

Fig. 12. Torque and stress diagram with the head at the bottom

As shown in Figure 12, the maximum torque of the circumferential and lifting motors is 11.3 N·m and 2.24 N·m, respectively. Additionally, the maximum torque that the deflection motor must overcome to remain stationary is about 0.13 N·m, below the rated torque. The maximum force exerted on the roller bearing during circumferential movement is approximately 415 N, and the maximum force acting on the driving wheel during lifting movement is around 292.4 N. Both forces are less than the theoretical values of 496.5 N and 302.2 N, respectively.

4. Experimental verification

The experiment utilizes a 508-mm-diameter pipe as the experimental object, as shown in Figure 13. First, the smoothness of movements in all four directions is assessed to determine whether each motor meets the actual load requirements and whether the electronic control program is accurate and functional.

Fig. 13. Experimental site

In verifying circumferential movement, the head remains stable at low speeds, with no noticeable vibration or resonance when the motor stops. The measured sliding distance for circumferential movement is 208 mm. During the verification of axial movement, the screw smoothly pushes the head at a slow speed without dragging or vibrating. The sliding distance for axial movement is 98 mm. In the verification of lifting movement, the meshing of the gear and rack is smooth, with no significant jamming or shaking, and the lifting stroke measures 34.8 mm. The maximum feed is 23.2 mm. The verification of deflection movement demonstrated that the pinion gear successfully drove the large gear to achieve a 5° deflection of the grinding motor, which can be fixed in position afterward, meeting the specified requirements.

Finally, the test cutting demonstrated that the grinding motor operated stably, reducing the previous operating time by 40%. Additionally, the cutting results were satisfactory, as shown in Figure 14.

Fig. 14. Result of cutting and grinding the pipe

The axial sliding distance has been reduced to 98 mm compared to the design calculations. This reduction is primarily attributed to structural optimization, which shortened the member by 68 mm. The experimental results indicate that all operational parameters remain within a reasonable range. No noticeable motor overload or inability to rotate was observed throughout the experiment, and no significant vibrations were detected. Additionally, no deformation of the components occurred during the cutting process, confirming the accuracy of the preliminary finite element analysis and kinematic simulation.

5. Conclusions

This study addresses the critical challenges of inefficiency and precision deficiency in conventional cutting and grinding processes for large-diameter pipes. Based on the research findings, the following conclusions can be drawn:

1. The rack reinforcement through rib augmentation and dimensional adjustment of critical components (centering rod: 600 mm, screw: 350 mm, support rod: 350 mm, support rod diameter: 12 mm) not only overall reduce material consumption but also enhance structural reliability.

2. Kinematic simulation analysis indicates that each motor's torque and the stress on key components meet the operational requirements. In the future, parameter optimization (e.g., tooth ratio or motor selection) can be explored to reduce energy consumption while ensuring accuracy.

3. The experiments demonstrate operational smoothness, precise positioning, and high efficiency of the motors, with cutting and grinding quality meeting welding specifications. A 40% reduction in operating time was achieved compared to the conventional methods. Further verification of the device's applicability with various pipe diameters and material types can be performed.

4. The successful development of this device has established a basis for the application of automated control in pipe engineering. Subsequently, it is essential to develop machine learning-based adaptive control algorithms and introduce vision-based sensing systems to adjust cutting and grinding parameters dynamically in real-time. These coordinated technological enhancements will ensure cutting and grinding precision while significantly boosting construction efficiency.

REFERENCES

[1] *MyoungHo Kim, Sung-Uk Lee, Sung-Soo Kim,* Real-Time Simulator of a Six Degree-of-freedom Hydraulic Manipulator for Pipe-cutting Applications, IEEE Access, Vol. **9**: 1, 2021.

[2] *Liwen Cao, Shuaitong Miao,* Design and Experimental Study of Wire Saw Machine for Cutting Oil Pipeline, IOP Conference Series: Materials Science and Engineering, Vol. **746**: 012036, 2020.

[3] *Xiao Deng, Tianyan Bai, Yuxiang Cui, Zhi Li, Yiming Mao, Weiping Ma,* Review on the Methods for Predicting the Residual Lifespan of Pipelines with Corrosion Defects, Petroleum and New Energy, Vol. **33(05)**: 28-32, 2021.
[4] *Zhenjun Bai,* Discussion on Selection of Welding Method for Pipe Replacement Emergency Repair of Long Distance Pipeline, Petro & Chemical Equipment, Vol. **25(06)**: 93-94, 2022.
[5] *Yao Ren, Robert Skilton,* A review of pipe cutting, welding, and NDE technologies for use in fusion devices, Fusion Engineering and Design, Vol. **202**: 114396, 2024.
[6] *Zhaozhi Wang,* Construction Technology Analysis of Mountain Pipe Trench of Oil and Gas Pipeline, Total Corrosion Control, Vol. **37(04)**: 64-66, 2023.
[7] *Daoyan Ying, Xiaoying Tang, Zihan You, Xinping Yu,* Analysis of Many Cognitive Misunderstandings and Blind Zone about Welding in Pressure Pipeline Engineering (1)-Welding Joint, Process Equipment and Piping, Vol. **61(04)**: 85-91, 2024.
[8] *Liang Cai,* Discussion on Key Technology of On-Line Welding for Long Distance Pipeline, Technology Supervision in Petroleum Industry, Vol. **40(07)**: 28-33, 2024.
[9] *Donato Sorgente, Rocco Salvato, Christian Bachmann, Curt Gliss, Günter Janeschitz, Hongtao Pan, Xinliang Zhou, Haoying Wang, Rocco Mozzillo,* Overview of in-bore pipe cutting and welding tools for the maintenance of CFETR and EU-DEMO, Fusion Engineering and Design, Vol. **203**: 114478, 2024.
[10] *Xiao Cheng, Jiangzhong Qian, Changwan Zheng, Fengxiang You, Haixia Wang, Jianfa Zhang, Shaolong Kuang,* A Fuzzy Adaptive PID Control Method for Novel Designed Rail Grinding Equipment, IEEE Access, Vol.**11**: 118-124, 2023.
[11] *Zhiyong Niu, Liang Cai, Shanglin Cui,* Discussion on Key Technologies of In-service Pipeline Welding Process, Petro & Chemical Equipment, Vol. **25(07)**: 134-136, 2022.
[12] *Fred Weinkam,* Inside Pipe Cutter Lock, Patent Application, USPTO 20190184476, 2019.
[13] *Huamei Bai, Yu Bai, Yanhong Gong, Yanfei Xu, Hongjing Liu, Junli Qiang,* Exploration and practice on energy conservation and consumption reduction of electric variable-frequency beveling machine, Energy Conservation in Petroleum & Petrochemical Industry, Vol. **13(04)**: 48-51, 2023.
[14] *A. G. Demeissie, Zheng Yu, Yang Yang,* Design of a novel grinding end-effector for spiral welded pipe, Journal of Physics: Conference Series, Vol. **1780(1)**: 012008, 2021.
[15] *Xianfeng Zhang,* Application of Magnetic Fixed Ground Wire Device in Oil and Gas Pipeline Welding, Chemical Engineering Management, Vol. **(26)**: 83-85, 2023.
[16] *Bruno Maric, Alan Mutka, Matko Orsag,* Collaborative Human-Robot Framework for Delicate Sanding of Complex Shape Surfaces, IEEE Robotics and Automation Letters, Vol. **5(2)**: 2848-2855, 2020.
[17] *Vazquez-Santacruz, J. A., Portillo-Velez, R., Torres-Figueroa, J., Marin-Urias, L. F, Portilla-Flores, E.,* Towards an integrated design methodology for mechatronic systems, Research in Engineering Design, Vol. **34(4)**: 497-512, 2023.